1   **Trajectory encounter number as a diagnostic of mixing potential in fluid flows**

2   Irina I. Rypina[1] and Larry J. Pratt[1]

3   [1] Woods Hole Oceanographic Institution, Physical Oceanography department,
4   266 Woods Hole rd., Woods Hole MA, 02543

5   Corresponding author email: irypina@whoi.edu

6   Abstract

7   Fluid parcels can exchange water properties when coming in contact with each other, leading to
8   mixing. The trajectory encounter number, which quantifies the number of fluid parcel trajectories
9   that pass close to a reference trajectory over a finite time interval, is introduced as a measure of
10   the mixing potential of a flow. Regions characterized by low encounter numbers, such as cores
11   of coherent eddies, have low mixing potential, whereas turbulent or chaotic regions characterized
12   by large encounter numbers have high mixing potential. The encounter number diagnostic was
13   used to characterize mixing potential in 3 flows of increasing complexity: the Duffing Oscillator,
14   the Bickley Jet, and the altimetry-based velocity in the Gulf Stream Extension region. An
15   additional example was presented where the encounter number was combined with the u-star-
16   approach of Pratt et al., 2016 to characterize the mixing potential for a specific tracer distribution
17   in the Bickley Jet flow. Analytical relationships were derived connecting encounter number to
18   diffusivity for purely-diffusive flows, and to shear and strain rates for linear shear and linear
19   strain flows, respectively. It is shown that in a diffusive regime the encounter number grows as a
20   square-root of time, whereas in a linear shear and strain flows the encounter number is
21   proportional to time.

22   I.   Encounter number
23   a. main idea

24   Mixing is an irreversible exchange of properties between different water masses. This process is
25   important for maintaining the oceanic large-scale stratification and general circulation, and it
26   plays a key role in the redistribution of bio-geo-chemical tracers throughout the world oceans.
27   Mixing occurs between different water masses when they come in direct contact with each other.
28   Thus, mixing potential of the flow, i.e., the opportunity for mixing to occur, is generally
29   enhanced in regions where water parcels meet or encounter many other water parcels, such as,
30   for example, within a chaotic zone –a region of the flow that is in a state of chaotic advection.
31   There, the separation between initially nearby water parcels grows exponentially in time and, in
32   the infinite time limit, each water parcel encounters all the other water parcels within the same
33   zone. Similarly, high encounter numbers will exist in turbulent regions. In contrast, mixing
34   potential is expected to be smaller in regions where water parcels do not experience many
35   encounters with other water parcels and remain close to their initial neighbors as the flow
36   evolves. This would be the case, for example, for a water parcel that is located inside a coherent

37   eddy. If the eddy is in a state of solid body rotation, the water parcel would forever stay close to

38   its initial neighbors and will not have any new encounters at all. If some amount of azimuthal

39   shear is present within the eddy, then for a water parcel located at a radius r from the eddy

40   center, encounters will be limited to those water parcels located within a circular strip centered at

41   the same radius r. Of course, the presence of a mixing potential does not guarantee that the

42   mixing of a tracer will occur: it is also essential that the tracer distribution is non-uniform, so that

43   irreversible property exchange can take place between different water parcels during their

44   encounters. Thus, the intensity of mixing would depend on both the tracer distribution and the

45   flow, whereas mixing potential is the property of only the flow field alone.

46   In this work we introduce an objective measure of encounters between different fluid elements in

47   order to quantify the mixing potential of a fluid flow. There are many existing trajectory-based

48   measures of fluid stirring; ours has the virtue of being easy to implement and immediately

49   applicable to ocean float and drifter data. Our method does not require the initial spacing

50   between trajectories to be small (as in Lyapunov exponent – based measures) and does not

51   require sophisticated book keeping as in braid theory (Allshouse and Thiffeault, 2012) or finite-

52   time entropy (Froyland and Padberg-Gehle, 2012).

53   b.   definition and numerical implementation

54   For a given reference trajectory, $\vec{x}(\vec{x}_0, t_0; t)$, the encounter number, $N(\vec{x}_0, t_0; t)$, is defined as a

55   number of trajectories starting at the same initial time t_0 that come within a radius R of the

56   reference trajectory over a time interval t. Here t is the trajectory integration time and $\vec{x}_0$ is the

57   trajectory initial position, i.e., $\vec{x}(\vec{x}_0, t_0; t = 0) = \vec{x}_0$. Regions of space with large/small N would

58   then be associated with enhanced/inhibited mixing potential.

59   We define $N(\vec{x}_0, t_0; t)$ based on the number of encounters with different trajectories, not the total

60   number of encounter events, so even if some trajectory first comes close to the reference

61   trajectory, then moves away and then re-approaches it again later, it is only counted once. In a

62   flow field with no sources or sinks of tracer variance, where variance is therefore decaying, it is

63   reasonable to expect that most property exchange will occur during the first encounter, thus the

64   motive for counting only this first encounter. If tracer variance is being continuously introduced,

65   it may be more reasonable to count the total number of encounters. Even so, the number of first

66   encounters still yields of measure of exposure of a water parcel with other parcels and therefore

67   should still be relevant.

68   For a numerical implementation of the trajectory encounter number-based mixing

69   characterization, one would need to start, at some time t_0, with a grid of initial positions

70   spanning the flow domain, and then evolve trajectories under the flow field over the time interval

71   t. This time interval should be chosen based on the physical properties of the flow and with

72   specific scientific questions in mind. For example, if the research focus is on ocean submesoscale

73   dynamics, the time scale t would be on the order of hours to days, whereas the corresponding
74   time scale for mesoscale dynamics would be on the order of weeks to months.

75    $N(\vec{x}_0, t_0; t)$ is a Lagrangian quantity that characterizes mixing potential of a flow over a time
76   interval from t_0 to $t_0 + t$. As the flow field evolves in time, its mixing characteristics can change
77   and $N(\vec{x}_0, t_0; t)$ will reflect this change. For example, if a coherent eddy with weak mixing
78   potential, embedded in a chaotic zone with enhanced mixing potential, was present in the flow
79   from time t_1 to time t_2, but it dispersed and disappeared afterwards, then $N(\vec{x}_0, t_0; t)$ is expected
80   to be small at those locations $\vec{x}_0$ that correspond to the interior of an eddy for $t_0 \geq t_1$ and
81    $t_0 + t \leq t_2$, whereas for $t_0 > t_2$, when the eddy is no longer present, $N(\vec{x}_0, t_0; t)$ would
82   increase. Dependences on t and t_0 are also expected to be present within a chaotic zone.
83   Although in the infinite time limit, all parcels will encounter all other parcels in a chaotic zone
84   and $N(\vec{x}_0, t_0; t \rightarrow \infty)$ would approach a constant, encounter rates over a finite time interval t are
85   locally the largest near a hyperbolic trajectory and along the segments of its associated stable
86   manifolds, which serve as pathways that bring water parcels into the vicinity of the hyperbolic
87   trajectory. Since locations of hyperbolic trajectories and manifolds generally evolve in time,
88    $N(\vec{x}_0, t_0; t)$ is expected to also vary with t_0. As the trajectory integration time t increases, water
89   parcels initially located further from the hyperbolic trajectory will have the opportunity to come
90   into its vicinity along the stable manifold. Such parcels, as they approach the hyperbolic
91   trajectory, are expected to have more encounters than their neighbors that are initially located off
92   the manifold and thus bypass the vicinity of the hyperbolic trajectory where many encounters
93   occur. Thus, $N(\vec{x}_0, t_0; t)$ will reveal longer segments of stable manifolds for longer integration
94   times t, as will be illustrated numerically in the next section. This is similar to how the
95   maximizing ridges of the forward time finite-time Lyapunov exponent field, which are often
96   used to approximate stable manifolds of hyperbolic trajectories, elongate and sharpen with
97   increasing integration time (Haller, 2002; Shadden et al., 2005; Lekien and Ross, 2010).

98   The radius R, which defines how close to a reference trajectory should another trajectory come in
99   order to be counted as an encounter, is an important parameter for the calculation of the
100   encounter number N. Generally, R should be small compared to the spatial scale of the smallest
101   features of interest. Specifically, for the N field to delineate a flow feature, say, an eddy,
102   trajectories within the eddy interior should not encounter those on its exterior. The boundary
103   region near the eddy perimeter, where such encounters can occur, has the width $2R$. So, if that
104   width is comparable to or larger than the eddy size, then the eddy would get completely smeared
105   out and will not be resolved. From a practical viewpoint, however, using very small R would
106   require very dense grids of trajectories to be computed, otherwise zero or very small number of
107   trajectory encounters will occur in the entire flow domain. Numerical examples in the next
108   section suggest that choosing R to be a fraction, up to about half of the size of the smallest
109   features of interest work best.

110   Once the time scale t is identified, trajectories are computed, and radius R is chosen, the number

111   of encounters, $N(\vec{x}_0, t_0; t)$, needs to be counted for each trajectory and plotted as a function of

112   the trajectory initial position $\vec{x}_0$. The resulting N field will delineate the flow regions with

113   different mixing properties as subdomains having different values of N.

114   II.   Examples

115   We proceed to test the performance of the encounter number technique in quantifying mixing

116   potential for several geophysically relevant sample flows of increasing complexity, starting from

117   a simple analytically prescribed periodically perturbed double-gyre Duffing Oscillator system,

118   followed by a dynamically consistent solution of the PV conservation equation on a beta-plane

119   known as the Bickley Jet, and finishing with an observationally based geostrophic velocity field

120   in the North Atlantic derived from the sea surface height altimetry.

121   a.   Duffing Oscillator

122   The Duffing Oscillator flow and its figure-eight geometry has become a standard test case for

123   emerging techniques related to the dynamical systems theory. This flow consists of two gyres

124   with the same sign of rotation (clockwise in our case), whose elliptic centers oscillate in time

125   around their mean position. A hyperbolic point is located at the origin between the two gyres,

126   and a pair of stable and unstable manifolds emanate from it forming a figure eight in the absence

127   of the time dependent perturbation, or forming a classic homoclinic tangle in the presence of the

128   perturbation. The velocity field is two-dimensional and incompressible and is given by $u = y$

129   and $v = (x - ax^3)\big(1 + \epsilon \cos(\omega t + \phi)\big)$ with $a = 1$, $\omega = 3\pi/2$, $\phi = \pi/4$ and $\epsilon = 0.1$. With

130   these parameters, the Poincare section (Fig. 1 bottom) shows the presence of two main regular

131   elliptic regions with O(1) radius corresponding to the interiors of the gyres, which are embedded

132   into a figure-eight shaped chaotic zone, within which a number of island chains with smaller

133   regular islands are present. The winding time for most trajectories in the system is on the order of

134    $5T_{pert}$ with $T_{pert} = \frac{2\pi}{\omega}$, except for trajectories near the hyperbolic point for which winding time

135   is much longer (Fig. 1 top).

136   The encounter number was computed for a range of trajectory integration times, from $T = T_{pert}$

137   (which is significantly shorter than trajectory winding time) to $T = 50T_{pert}$ (significantly longer

138   than trajectory winding time), and for a range of encounter radii, from $R = 0.01 \ll R_{eddy}$

139   (significantly smaller than the eddy core radius) to $R = 1 \approx R_{eddy}$ (comparable to the eddy core

140   radius). The results in Fig. 2 suggest that the encounter number method works best for

141   integration times longer than the trajectory winding time and encounter radius about 1/3 to 1/2 of

142   the gyre radius (right 3 panels of the middle row). For very small encounter radius (top row), N

143   is noisy because trajectories simply do not encounter many neighbors. Thus, delineating the

144   domain into regions with different mixing potential, as in the top right panel, requires long

145   integration time. For $T = 50T_{pert}$, good agreement with Poincare section is observed, and the

146   use of small encounter radius allows for a precise identification of smaller regular island chains,
147   such as the chains of 4 islands located just outside of the perimeter of both left and right eddy
148   cores. Note that the noise in the N field can be suppressed by using a denser initial grid of
149   trajectories, but at the cost of a more expensive computation. For very short integration times
150   (left column) when trajectory segments are very short, the encounter number is not capturing the
151   difference between the regular and chaotic regions. This is not surprising as velocity shear is
152   probably a dominating factor over such small times. As the integration time increases, the
153   difference in encounter number becomes more pronounces between trajectories that remain
154   within the eddy cores and trajectories that are free to move around the chaotic zone. Over a time
155   scale of approximately one winding period (or about 5 periods of the perturbation; second
156   column), the two regular eddy cores (blue regions with small N) and a segment of the stable
157   manifold (red curve emanating from the origin with largest N) becomes clearly visible for R=0.2
158   and R=1. The revealed manifold segment becomes longer, narrower and more tangled,
159   eventually filling up the whole chaotic zone. At the same time, the shape of the core region
160   becomes more exact and approaches the "true" core in the Poincare section as the integration
161   time increases to 50 periods of the perturbation. The agreement with Poincare section is excellent
162   in the right middle panel, although the smaller island chains are not as visible as in the top right
163   panel because of the use of a larger encounter radius that is comparable to their size (see Fig. 3).
164   Finally, for the large encounter radius that is comparable to the size of the eddy (bottom row),
165   the boundary region near perimeter of an eddy, within which trajectories on the inside of the
166   eddy can encounter trajectories passing by on the outside, is as wide as the eddy itself, essentially
167   wiping out all small scales from the N field. All of these trends are in agreement with theoretical
168   expectations described in Section I.

169   b.   Bickley Jet

170   The meandering Bickley jet flow is an idealized, but linearly dynamically consistent, model for
171   the eastward zonal jet in the Earth's Stratosphere (Rypina et al., 2007a; Rypina et al., 2011).
172   This flow consists of a steady eastward zonal jet on which two eastward propagating Rossby-like
173   waves are superimposed. All flow parameters used here are identical to those used in our
174   previous 2007 and 2011 papers. In the reference frame moving at a speed of one of the waves,
175   the flow consists of a steady background velocity subject to a time periodic perturbation. The
176   background looks like a meandering jet, with three recirculation gyres to the north and south of
177   the jet core. Between the recirculation gyres, there are three hyperbolic points with the associated
178   stable and unstable manifolds. Under the influence of the time-periodic perturbation imposed by
179   the second wave, heteroclinic tangles are formed by the manifolds emanating from different
180   hyperbolic regions between the recirculations, and a chaotic zone emerges on either side of the
181   jet. The manifolds, however, cannot penetrate through the jet core, which remains regular and
182   acts as a transport barrier separating the northern and southern chaotic zones. All of these
183   features are clearly visible in the Poincare section shown in Fig. 4 (top). The bottom subplot
184   shows the N field computed using the encounter radius $R=5*10^5$, which is about half of the

185 recirculation region radius, and using trajectory integration time on the order of a few winding
186 times within the recirculations. As expected, the encounter number identified 6 recirculation
187 regions and the jet core as zones with small mixing potential (blue). 6 blue recirculation regions
188 are embedded into two distinct chaotic zones with enhanced mixing potential (yellow-red) on
189 either side of the jet. Mixing potential is the largest (red) along the segments of stable manifolds
190 emanating from the hyperbolic trajectories between recirculations.

191   c.   Altimetry-based velocity in the meandering Gulf Stream region

192 The flow in the Gulf Stream Extension region, with a non-steady meandering jet that sheds
193 coherent eddies and recirculations to the north and south, has a lot in common, at least
194 qualitatively, with the Bickley Jet example. Unlike the idealized model, however, the real
195 oceanic eddies have finite lifetimes, and the jet is not periodic in the zonal direction.
196 Nevertheless, many of the qualitative features of the Bickley Jet's N field hold in this example.
197 Specifically, trajectories inside coherent eddy cores have smaller encounter number than their
198 surroundings, and the jet centerline has smaller encounter number than the flanks.

199 The velocity field that we used was downloaded from the AVISO website
200 (http://www.aviso.altimetry.fr/en/data/products/sea-surface-height-products/global.html) and
201 corresponds to their gridded product with ¼ deg spatial resolution and temporal step of 1 day.
202 This velocity is based on the altimetric sea surface height measurements made from satellites.
203 The heights were converted into velocities using geostrophic approximation. For the encounter
204 number estimation, trajectories were seeded on a regular grid with $dx = dy \cong 0.06$ deg on 11
205 July 1997 and were integrated forward in time for 90 days using a fifth-order variable-step
206 Runge-Kutta integration scheme with bi-linear interpolation between grid points in space and
207 time. The encounter radius was chosen to be 0.3 deg, which is about a third of the radius of a
208 typical 200-meter-wide Gulf Stream ring.

209 The encounter number was estimated for three different integration times, T= 30 days, 60days
210 and 90 days (Fig. 5). The N field reveals that a number of coherent eddies were present on both
211 sides of the meandering jet on 11 July 1997. Among those, two strongest ones can be seen at
212 54W, 36N and 52W, 41N, with the low-N (blue) core and high-N (red) perimeter. As the
213 integration time increases from 30 days to 90 days, the eddies start to leak fluid, their cores start
214 to lose coherence, and the encounter number within the eddy core starts to increase as more and
215 more trajectories escape into the eddy surroundings over time. To visualize this behavior, we
216 extracted trajectories from the core of the northern eddy in Fig. 5(left) (i.e., trajectories with
217 N<100 from the 30-day-long N field), and plotted their subsequent positions after 30 days, 60
218 days and 90 days. The results in Fig. 6 confirm that the eddy core stays completely coherent over
219 30 days (i.e., all trajectories stay together), but starts to deteriorate at 60 days, with only a small
220 fraction of the initial patch still staying together and the rest of the patch dispersing and forming
221 long and narrow filaments.

222   The jet region, although noisy, seems to suggest higher N near the flanks and smaller near the
223   centerline. The center region is not as well-defined as in the Bickley Jet example, possibly
224   because the Gulf Stream inhibits but does not fully prevent the meridional transport in this
225   region, and because our encounter radius might have been too large to reveal the central region,
226   if the true center region was narrower than 2R (0.6 degrees). Finally, the N field suggests that the
227   mixing potential of the flow is not symmetric with respect to the jet centerline and is higher on
228   the northern side. It would be interesting to see if this is a general property of the flow in this
229   region or if this phenomenon is specific to the time interval chosen. This investigation is left for
230   future study.

231   III.   Connection between the encounter number and diffusivity, shear and strain rate for a
232   diffusive, linear shear and linear strain flows, respectively

233   By analogy with molecular diffusion, eddy diffusivity is often used to characterize the eddy-
234   induced downgradient tracer transfer in realistic geophysical fluid flows. Because of the
235   simplicity of this approach, the majority of existing non-eddy-resolving oceanic numerical
236   models are diffusion based, despite the somewhat questionable assumptions underlying this
237   approach.

238   A connection between the encounter number and diffusivity (LaCasce 2008; Vallis, 2006;
239   Rypina et al., 2015; Kamenkovich et al., 2016) can be derived under the assumption of a
240   diffusive random walk particle motion, where the root-mean-square (RMS) distance from
241   particle's initial position grows in time, on average, in proportion to $r_{RMS}(t) \sim \sqrt{Kt}$ with K
242   denoting the diffusivity. To derive the expression for the encounter number for such process, it is
243   convenient to move to a reference frame that is tied to a reference particle, which would then
244   always stay at the origin, while other particles would be involved in a random walk motion. Over
245   a time interval t, those particles that are located within a circular strip between radii R and
246   R+$r_{RMS}(t)$ will have a chance to encounter the reference particle, i.e., to enter into a circle of
247   radius R around the origin. For particles released on a regular grid with spacing dx and dy
248   between the neighbors in the x and y directions, respectively, the number of particles within such
249   circular strip is $n = \frac{S}{dxdy}$ where S is the area of the strip. Not all of the particles within this
250   circular strip, however, will necessarily move toward the origin; some will move away and thus
251   will not encounter the reference particle. Since the random walk process does not have a
252   preferred direction, for a particle located at a distance r from the origin, the probability to move
253   towards the reference particle and enter into a circle of radius R, as opposed to bypassing this
254   circle, is $P(r) = \frac{\alpha}{\pi} = \frac{Arcsin\left(\frac{R}{r}\right)}{\pi}$ where α is the angle between the direction to the origin and the
255   tangential direction to the circle of radius R, as indicated in Fig. 7. The encounter number for our
256   reference particle can then be written as

$$N = \frac{1}{dxdy}\int_0^{2\pi} d\theta \int_R^{R+r_{\text{RMS}}} rP(r)dr = \frac{2}{dxdy}\int_R^{R+r_{\text{RMS}}} rArc\sin\frac{R}{r}dr =$$

257

$$= \frac{1}{dxdy}\left[rR\left(1-\frac{R^2}{r^2}\right)^{1/2} + r^2 ArcSin\frac{R}{r} \right]\Bigg|_R^{R+r_{\text{RMS}}} \xrightarrow{r_{\text{RMS}}\to\infty} \frac{2}{dxdy} rR\Bigg|_R^{R+r_{\text{RMS}}} \sim \frac{2R\sqrt{Kt}}{dxdy},$$

(1)

258

259   where the last two expressions correspond to a long time limit.

260   The ballistic spreading that is dominated by a local velocity shear is another commonly-
261   encountered spreading regime. There, the separation between particles grows in proportion to
262   time. Ballistic spreading can often be observed in nonsteady realistic oceanic flows at time scales
263   that are much shorter than the onset of diffusive spreading (which develops after a trajectory
264   samples multiple different eddies or other flow features). To derive a connection between
265   encounter number and velocity shear, consider a trajectory that is advected by a flow field with
266   linear meridional velocity shear, γ, of zonal velocity. In a reference moving with a reference
267   trajectory the velocity profile is, $u(y) = \gamma y$ where u denotes the x-component of velocity, and
268   the encounter number becomes

269    $$N = \frac{2}{dxdy}\int_0^R dy \int_R^{R+x(t)} dx = \frac{2}{dxdy}\int_0^R dy \int_0^t u(y)dt = \frac{\gamma R^2 t}{dxdy},$$ (2)

270   suggesting a faster linear growth with time for a ballistic regime, compared to a slower square-
271   root dependence for purely diffusive motion.

272   The steady linear saddle flow with a constant strain rate α and velocities

273    $$u = \alpha x; v = -\alpha y.$$ (3)

274   is another commonly-considered example often used to approximate the vicinity of a hyperbolic
275   trajectory in more complicated non-steady non-linear situations. A unique property of this flow is
276   that the velocity profile is unchanged in any reference frame moving with a trajectory. This can
277   be shown by applying the coordinate transformation, $\hat{x} = x - x_{tr}(t); \hat{y} = y - y_{tr}(t)$, where
278    $(x; y)$ are coordinates in a stationary frame, $(\hat{x}; \hat{y})$ are coordinates in a moving frame, and
279    $(x_{tr}(t); y_{tr}(t))$ is the trajectory. The velocity in a moving frame is then

280
$$\hat{u} = u - \frac{dx_{tr}}{dt} = \alpha x - \frac{dx_{tr}}{dt} = \alpha\hat{x} + \alpha x_{tr} - \frac{dx_{tr}}{dt} = \alpha\hat{x}$$
$$\hat{v} = v - \frac{dy_{tr}}{dt} = -\alpha y - \frac{dy_{tr}}{dt} = -\alpha\hat{y} - \alpha y_{tr} - \frac{dy_{tr}}{dt} = -\alpha\hat{y}$$
(4)

281   where the last equality holds because $\frac{dx_{tr}}{dt} = \alpha x_{tr}; \frac{dy_{tr}}{dt} = -\alpha y_{tr}$. Thus, without loss of
282   generality, we can consider a flow in a reference frame moving with a reference trajectory that is

283 located at the origin. The number of trajectories that come within a radius R of the origin over
284 the time interval T can be written as

285 $N = \frac{1}{dxdy}\int_0^T F_\perp(t)dt,$ (5)

286 where dx and dy denote the grid spacing between neighboring trajectories, and the flux of
287 trajectories entering the circle is given by

288 $F_\perp = \int u_\perp ds.$ (6)

289 Here $u_\perp$ is the inward-looking normal component of velocity at a circle of radius R, and ds is an
290 infinitesimal segment of the circle arc. From symmetry, the flux is the same in each of the 4
291 quadrants so we will consider the 1st quadrant only. From geometry (Fig. 7 (right)),

292 $u_\perp = -u\sin\beta - v\cos\beta = \alpha R(\cos^2\beta - \sin^2\beta)$ and $ds = Rd\beta$, leading to

293 $F_\perp^{1st\,quad} = \alpha R^2 \int_0^{\pi/4}(\cos^2\beta - \sin^2\beta)\,d\beta = \frac{\alpha R^2}{2}$ (7)

294 and

295 $N^{1st\,quad} = \frac{1}{dxdy}\int_0^T F_\perp(t)dt = \alpha R^2 T/2.$ (8)

296 Adding the other 3 quadrants then gives

297 $N = \frac{2\alpha R^2 T}{dxdy}.$ (9)

298 The linear growth of the encounter number with time in the linear shear and linear strain flows
299 could be anticipated by noting that both flows are steady in a reference frame moving with a
300 reference trajectory, and all particles only encounter the origin once and never come back. Thus,
301 the flux through the encounter circle is constant in time and the encounter number, which is a
302 time-integral of flux, is proportional to time. The random walk flow is different because the
303 particles can encounter the reference trajectory more than once, leading to a non-steady flux of
304 first encounters and a non- linear time dependence of the encounter number.

305 IV. Mixing potential for a specified tracer: the $\boldsymbol{u}^*$-approach

306 The above examples are centered on mixing potential of a flow field, but there may be value in
307 computing the encounter number for swarms of trajectories of biological organisms, drifting
308 sensors, and other non-Lagrangian trajectories. For example, if one is interested in the actual
309 transport of scalar properties such as heat, salt, or vorticity, then it may be useful to calculate N
310 using a velocity field that is directly linked to the vector flux of the scalar of interest. This

311   linkage is made explicit by Pratt et al. (2016), who define velocity field $\boldsymbol{u}^*$ based on the (known)
312   flux $\boldsymbol{F}$ of a scalar with concentration C. Here bold quantities denote vectors. The concentration is
313   assumed to obey a conservation equation of the form

314   $$\frac{\partial C}{\partial t} = -\nabla \cdot \boldsymbol{F} + S, \tag{10}$$

315   where S contains the sources and sinks of C. The velocity $\boldsymbol{u}^*$ is defined as the velocity of a
316   hypothetical flow in which the flux of C is purely advective: $\boldsymbol{F} = C\boldsymbol{u}^*$. It can be shown that, in
317   the absence of sources or sinks of C, that the total amount of C contained within any material
318   boundary advected by this hypothetical flow is conserved: $\frac{d}{dt}\int_V C dV = 0$. Thus $\boldsymbol{u}^*$ is linked to
319   scalar property fluxes while $\boldsymbol{u}$ is limited to fluid volume (or area) fluxes.

320   If indeed $\boldsymbol{F}$ is due entirely to advection by the actual fluid velocity field $\boldsymbol{u}$, then $\boldsymbol{u}^*=\boldsymbol{u}$, but more
321   generally $\boldsymbol{F}$ will contain contributions from eddy fluxes, molecular or sub-grid diffusion, and
322   even forcing and dissipation terms that can be expressed as the divergence of a flux. In addition,
323   $\boldsymbol{F}$ may be augmented by the addition of any non-divergent vector without altering Eq. (3).
324   Although this lack of uniqueness may seem troublesome, it provides a degree of flexibility that
325   can be exploited, as we demonstrate below. Thus, by estimating the encounter number N for
326   trajectories of the $\boldsymbol{u}^*$ field, one is quantifying the rate at which different tracer parcels are
327   brought into contact with each other. An example is presented next.

328   a.   Example: encounter number for a tracer with a specified initial distribution in a
329   Bickley Jet flow

330   In this subsection we apply the encounter number diagnostic to quantify the mixing potential for
331   a specific tracer in the Bickley Jet flow. Our goal is to describe an example where the $\boldsymbol{u}^*$ field for
332   a given tracer is significantly different from the flow velocity $\boldsymbol{u}$, and where the corresponding
333   encounter number field for a given tracer, N^*, is significantly different from the water particle
334   trajectory-based encounter number N.

335   Consider the Bickley Jet flow with the same parameters as in II(b) and assume that one is
336   interested in a tracer that is, at initial time t0, completely flat south of the jet and has a constant
337   meridional gradient north of the jet, i.e., $C_0 = c_0 + 0.5y(sign(y - 5 * 10^5) + 1)$ with $c_0 = 1$.
338   Ignoring the diffusive terms, the tracer evolution is governed by the advection equation $\frac{\partial C}{\partial t} =$
339   $-\nabla(\boldsymbol{u} \cdot C)$, where $\boldsymbol{u}$ is the Bickley Jet flow velocity. Since the jet core acts as a transport barrier
340   separating the northern and southern chaotic zones, this tracer will rapidly filament and develop
341   high property gradients north of the jet, but will remain flat south of the jet. So, despite the fact
342   that the mixing potential of the Bickley Jet flow is exactly the same on both sides of the jet (Fig.
343   3(bottom)), stirring will not lead to mixing for this particular tracer distribution south of the jet,
344   where tracer gradient is zero, thus leading to zero mixing potential for this particular tracer. We

345   seek to capture this effect via applying the encounter number-based mixing diagnostic to the
346   corresponding $\boldsymbol{u}^*$ field for this tracer.

347   In this example, it is most convenient to make use of the flexibility in the definition of the tracer
348   flux and define $\boldsymbol{F}$ to be the flux of a tracer anomaly with respect to the value south of the jet,
349   $\boldsymbol{F} = \boldsymbol{u} \cdot (C - c_0)$. This is allowed because the additional flux vector, $\boldsymbol{F_1} = -\boldsymbol{u}c_0$, is non-
350   divergent. The resulting $\boldsymbol{u}^* = \frac{\boldsymbol{F}}{C} = \boldsymbol{u}\left(1 - \frac{c_0}{C}\right)$ is zero south of the jet where $C = c_0$ and is
351   approximately equal to $\boldsymbol{u}$ north of the jet where $C \gg c_0$, leading to the $\boldsymbol{u}^*$-based encounter
352   number $N^* = 0$ south of the jet and $N^* \approx N$ north of the jet.

353   This behavior was further validated numerically in Fig. 8, where we first numerically simulated
354   the evolution of this tracer in the Bickley Jet flow, then estimated $\boldsymbol{u}^*$ and counted N^* for
355   trajectories advected by the $\boldsymbol{u}^*$ field. The result confirms that mixing potential for this tracer is
356   zero south of the jet, $N^* = 0$, whereas north of the jet N^* is very close to N from Fig. 4(bottom).
357   Thus, by combining the $\boldsymbol{u}^*$ approach of Pratt et al., 2016 with the encounter number idea, we
358   were able to correctly capture the mixing potential for a specific tracer.

359   V.   Summary and discussion

360   When water parcels come in direct contact with each other, they can exchange water properties,
361   leading to mixing. The trajectory encounter number, N, quantifies the number of fluid parcel
362   trajectories that pass close to a reference trajectory over a time interval T. Thus, the encounter
363   number is proportional to, and can be used as a measure of, the mixing potential of a flow.

364   The encounter number diagnostic was tested in 3 flows with increasing complexity, the Duffing
365   Oscillator, the Bickley Jet, and the altimetry-based velocity in the Gulf Stream Extension region.
366   In all cases, N was smaller within cores of coherent eddies and jets, where mixing potential was
367   low, and N was larger in chaotic zones near the perimeters of the eddies and at the flanks of the
368   meandering jets, where the mixing potential of the flow was high.

369   Similar to finite-time Lyapunov exponents (FTLEs) that are commonly used to delineate regions
370   with qualitatively different motion (Haller, 2002; Shadden et al., 2005; Lekien and Ross, 2010),
371   N depends on the trajectory starting time, t0, allowing tracking the evolution of oceanic features
372   by repeating the calculation at different t0, and on the trajectory integration time, T, revealing
373   different structures that impact the mixing potential of the flow from time t0 to time t0+T.
374   Specifically, longer segments of manifolds emanating from hyperbolic regions are revealed for
375   longer T. In the long-T limit, when manifolds fill in the entire chaotic zone, N approaches a
376   constant equaling to the number of trajectories initially released within the chaotic zone. N also
377   depends on the encounter radius R, which defines how close two trajectories need to be in order
378   to be counted as an encounter. Analytic arguments and numerical simulations both suggest that R
379   on the order of a fraction (~1/3) of the radius of the smallest feature of interest should work well
380   in most cases. Finally, the encounter number N depends on the initial spacing between

381   neighboring trajectories. For identifying regions with enhanced or inhibited mixing potential
382   within the same flow, such as coherent eddy cores, jet cores, manifolds and chaotic zones, this
383   dependence is not important, provided that the initial grid was regular and spacing was the same
384   throughout the entire domain. If needed, this dependence can be easily eliminated by
385   normalizing the encounter number by the number of initial neighbors within the encounter
386   radius. We did not implement this normalization in our examples.

387   As with FTLEs, complexity measures (Rypina et al., 2011), Lagrangian descriptors (Mendoza et
388   al., 2014) and other techniques from the dynamical systems theory (Beron-Vera et al., 2013;
389   Budisic and Mezic, 2012; Froyland et al., 2007; Haller et al., 2016), N can be computed for
390   forward and backward in time trajectories, with the backward computation revealing unstable
391   manifolds.

392   The analytic connection between trajectory encounter number and a widely-used measure of
393   mixing, the diffusivity K, was derived under the assumption of a purely-diffusive random walk
394   process, where it was shown that $N \propto \sqrt{Kt}$. On the other hand, for a ballistic spreading regime
395   dominated by the velocity shear γ, and for the linear saddle flow with a constant strain α, N was
396   shown to be proportional to γt and αt, respectively. The linear growth of the encounter number
397   with time for the linear shear and linear strain flows is a consequence of the steady flux of first
398   encounters through the encounter circle. The non-linear dependence for the diffusive flow is
399   caused by the repeated encounters of particles with a reference trajectory leading to the flux of
400   first encounters that decreases with time.

401   The mixing potential is the property of the flow field and characterizes the intensity of stirring,
402   whereas the actual tracer mixing depends both on the flow and the tracer. For example, no tracer
403   mixing will occur if the tracer gradient is zero, even if the mixing potential of the flow is high.
404   To address this, we have proposed combining the encounter number diagnostic with the $\boldsymbol{u}^*$-
405   approach of Pratt et al, 2016 for characterizing the mixing potential for a specific tracer C. $\boldsymbol{u}^*$
406   depends on, and includes information about, the tracer fluxes. In the absence of sources and sinks
407   of C, the amount of tracer is conserved within any Lagrangian volume advected by $\boldsymbol{u}^*$, so the
408   encounter number N^* computed for trajectories advected by $\boldsymbol{u}^*$ can be used to quantify the
409   mixing potential for a specific tracer. An example was presented where N^* for a specified tracer
410   distribution in the Bickley Jet flow was significantly different from N in a large part of the
411   domain.

412   The encounter number is a frame-independent quantity because it is based on relative distances
413   between water parcel trajectories, rather than on properties of isolated trajectories. The encounter
414   number values do not change under orthogonal transformations of coordinates, i.e., under
415   rotations and translations of a reference frame. This is a desirable property because the ability of
416   a flow to mix tracers should not depend on the reference frame.

417 The encounter number ideas presented in this paper are not restricted to two-dimensional flows
418 and do not require incompressibility, although all flow fields (except $\boldsymbol{u}^*$) considered here were
419 two-dimensional and incompressible. The encounter number can be used to quantify mixing
420 potential in three-dimensional flows, but this extension is left for a future study.

421 **Acknowledgments:** This work was supported by the NSF grants OCE-1154641, OCE-1558806
422 and EAR-1520825, ONR grant N00014-11-10087 and NASA grant NNX14AH29G.

423

424

425

426

427

428

429

430

431

432

433

434

435

436

437

438

439

440

441

442

443

References:

Allshouse, M. R. and J.-L.T., Detecting coherent structures using braids, *Physica D* **241** (2), 95–105, January 2012.

Beron-Vera, F. J., Wang, Y., Olascoaga, M. J., Goni, J. G., and G. Haller, "Objective detection of oceanic eddies and the Agulhas leakage," J. Phys. Oceanogr. 43, 1426–1438 (2013).

Budisic, M. and Mezic, I., "Geometry of the ergodic quotient reveals coherent structures in flows," Physica D 241, 1255–1269 (2012).

Froyland, G., Padberg, K., England, M. H., and Treguier, A. M., "Detection of coherent oceanic structures via transfer operators," Phys. Rev. Lett. 98, 224503 (2007).

Froyland, G. and K. Padberg-Gehle. Finite-time entropy: a probabilistic approach for measuring nonlinear stretching. *Physica D*, 241(19):1612-1628, 2012

Haller, G.: Lagrangian coherent structures from approximate velocity data, Phys. Fluid, 14, 1851–1861, 2002.

Haller, G., A. Hadjighasem, M. Farazmand and F. Huhn, 2016: "Defining coherent vortices objectively from the vorticity," J. Fluid Mech. (2016), vol. 795, pp. 136_173. doi:10.1017/jfm.2016.151

Kamenkovich, I., I. Rypina, and P. Berloff, 2015: Properties and Origins of the Anisotropic Eddy-Induced Transport in the North Atlantic. *J. Phys. Oceanogr.,* **45**, 778–791, doi: 10.1175/JPO-D-14-0164.1.

LaCasce, J. H., 2008: Lagrangian statistics from oceanic and atmospheric observations. Transport and Mixing in Geophysical Flows, J. B. Weiss and A. Provezale, Eds., Springer, 165–228.Cambridge University Press, 745 pp.

Lekien, F. and Ross, S. D.: The computation of finite-time Lyapunov exponents on unstructured meshes and for non- Euclidean manifolds, Chaos, 20, 017505, doi:10.1063/1.3278516, 2010

Mendoza, C., Mancho, A. M., and Wiggins, S., "Lagrangian descriptors and the assessment of the predictive capacity of oceanic data sets," Nonlinear Process. Geophys. 21, 677–689 (2014).

Pratt, L., R. Barkan, and I. Rypina, 2016: "Scalar flux kinematics," Fluids 2016, 1, 27; doi:10.3390/fluids1030027

Rypina, I. I., Scott, S. E., Pratt, L. J., and Brown, M. G., "Investigating the connection between complexity of isolated trajectories and lagrangian coherent structures," Nonlinear Proc. Geophys. 18, 977–987 (2011).

487 Rypina, I. I., Brown, M. G., Beron-Vera, F. J., Kocak, H., Olascoaga, M. J., and
488 Udovydchenkov, I. A.: On the Lagrangian dynamics of atmospheric zonal jets and the
489 permeability of the Stratospheric Polar Vortex, J. Atmos. Sci., 64, 3593–3610,
490 2007a.

491 Rypina, I., I. Kamenkovich, P. Berloff, and L. Pratt, 2012: Eddy-induced particle dispersion in
492 the near-surface North Atlantic. J. Phys.
493 Oceanogr., 42, 2206–2228, doi:10.1175/JPO-D-11-0191.1.

494 Shadden, S. C., Lekien, F., and Marsden, J. E.: Definition and properties of Lagrangian coherent
495 structures from finite-time Lyapunov exponents in two-dimensional aperidic flows, Physica D,
496 212, 271–304, 2005.
497
498 Vallis, G. K., 2006: Atmospheric and Oceanic Fluid Dynamics.
499
500
501
502
503
504
505
506
507
508
509
510
511
512
513
514
515
516
517

518
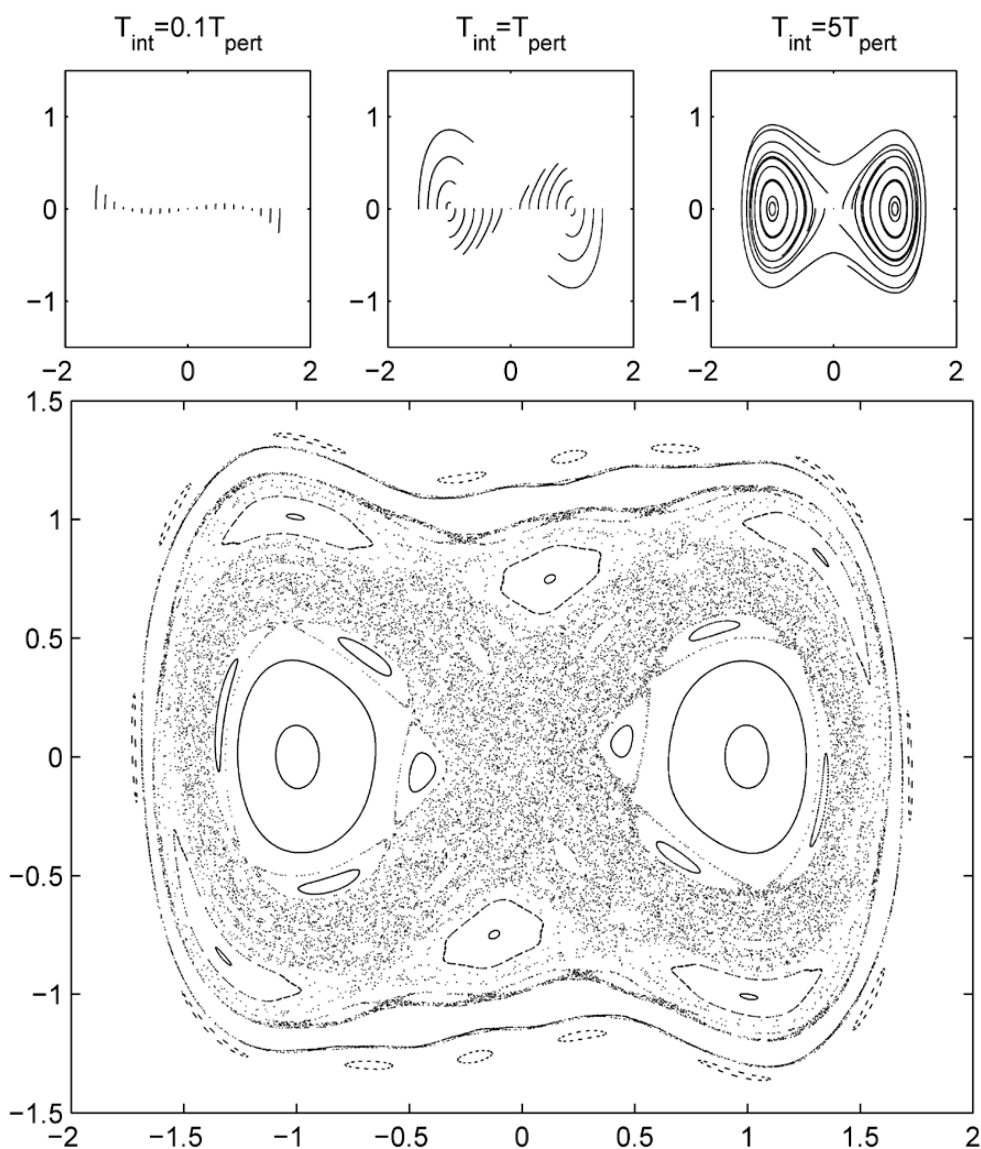
519
520 **Figure 1.** Trajectory segments for different integration times (top) and Poincare section (bottom) for the Duffing
521 Oscillator
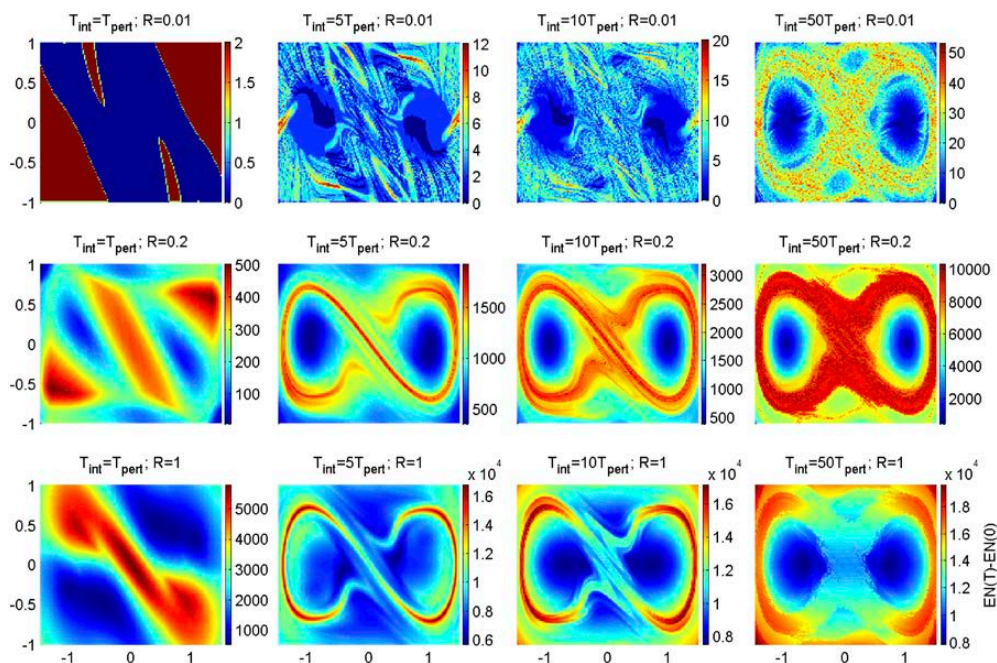
Figure 2. Encounter number for the Duffing Oscillator for various integration times, from T=0.1Tpert (on the left) to T=50Tpert (on the right), and for various encounter radii, from R=0.01 (on the top) to R=1 (on the bottom).

525
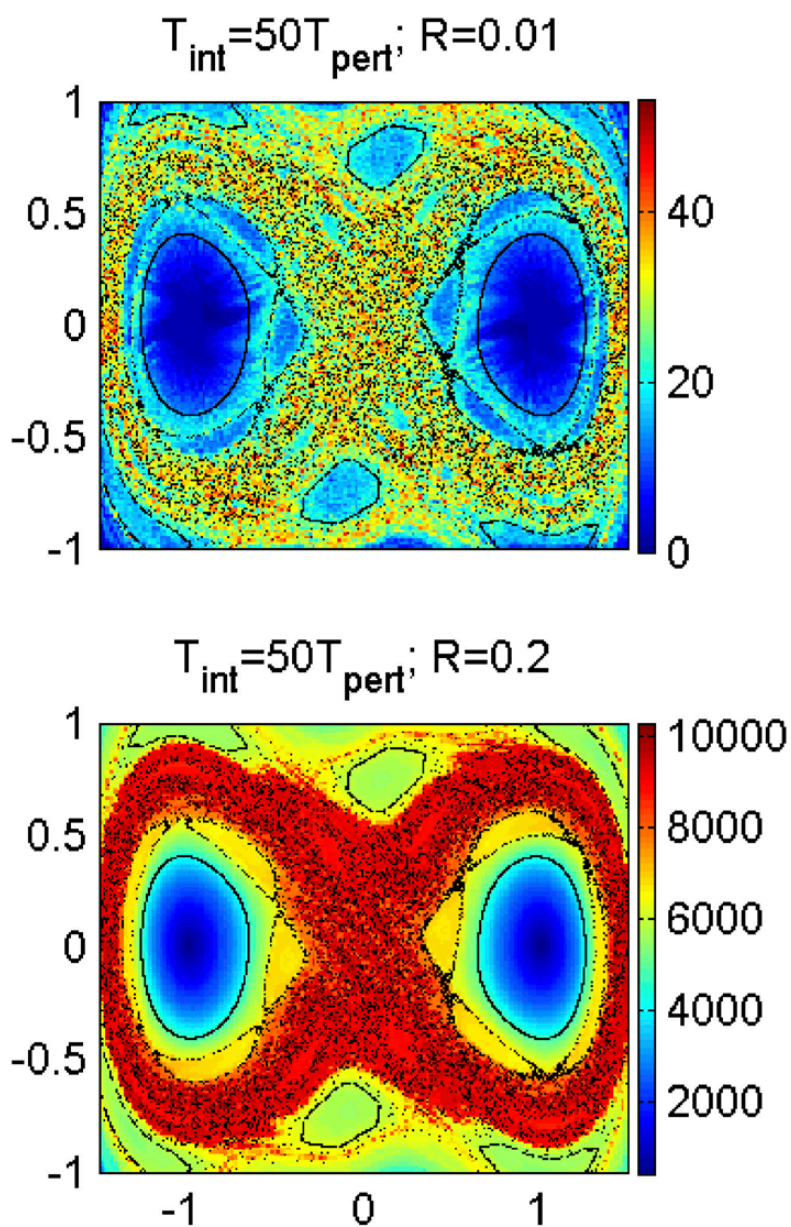
Figure 3. Poincare section (black dots; same as in the bottom panel of Fig. 1) superimposed onto the encounter number (color; same as top and middle right panels in Fig. 2). Only select trajectories from the Poincare section are shown.
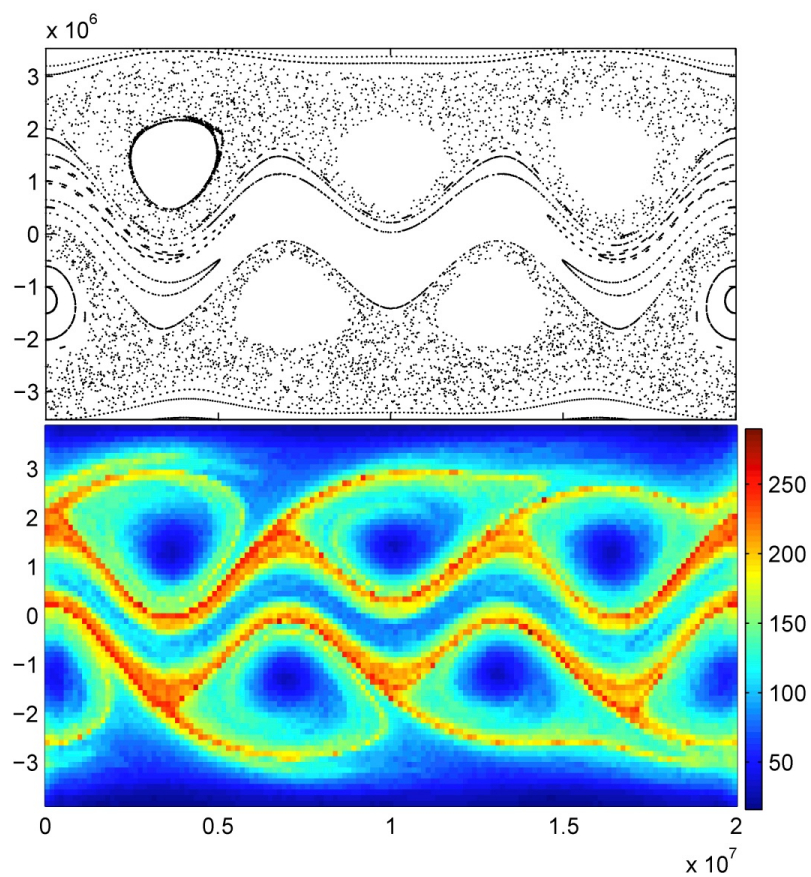
528

529   **Figure 4. Poincare section (top) and encounter number field N (bottom) for the Bickley Jet flow.**

530

531

532

533
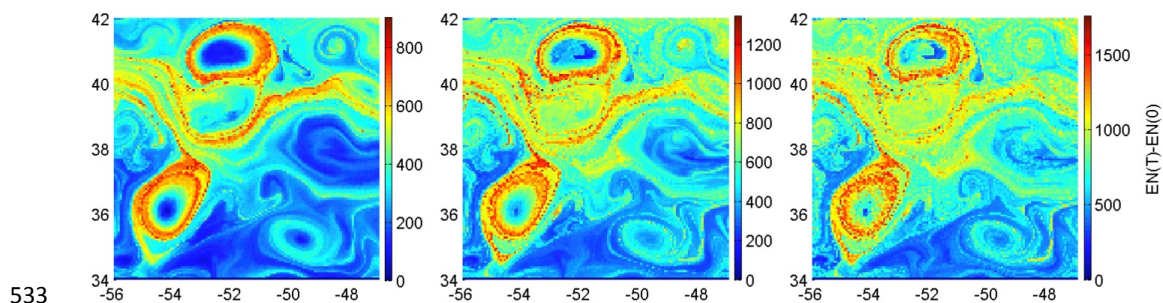
Figure 5. Encounter number on 7/11/1997 using AVISO velocities in the Gulf Stream Extension region for trajectory
integration time of 30 days (left), 60 days (middle) and 90 days (right).

536

537

538

539

540

541

542

543

544
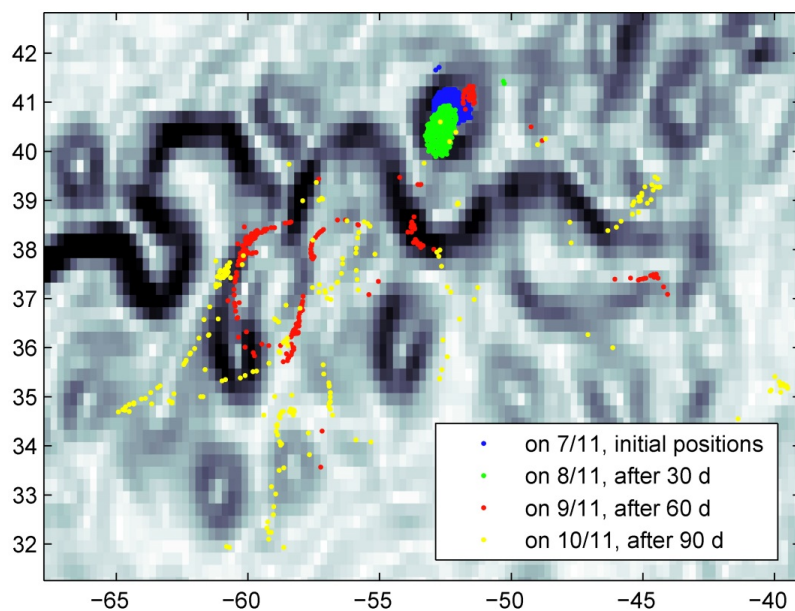
Figure 6. Positions of trajectories that were initially located within the eddy core on 7/11/1997 (blue patch) after 30 days (green), 60 days (red) and 90 days (yellow) of integration. Background shows the flow kinetic energy snapshot on 7/11/1997.

545
546

547

548

549
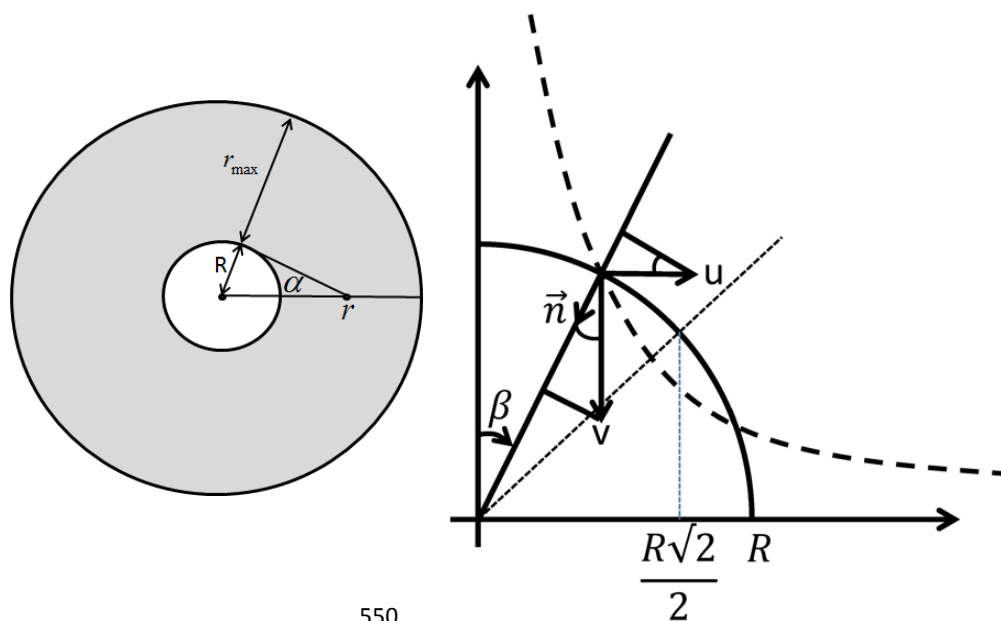
550   550

Figure 7. Schematic diagram for estimating encounter number for diffusive process (left) and for a linear saddle (right).

552

553

554

555
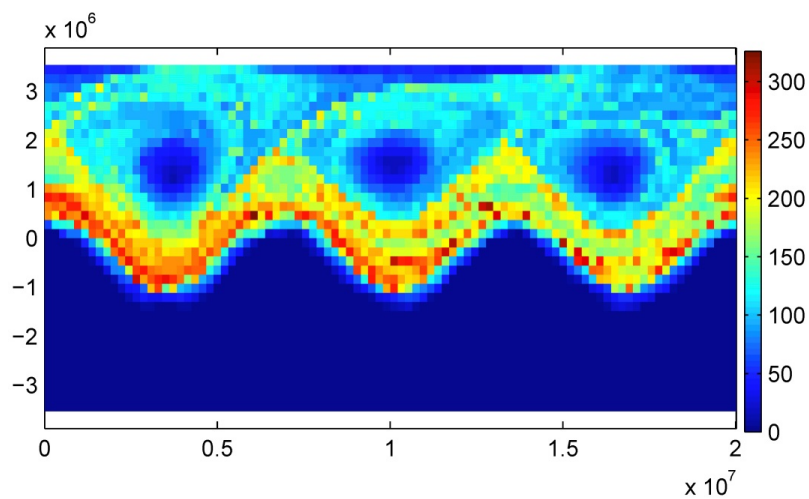
556

557   **Figure 8. U-star-based encounter number field Nstar for a tracer with flat initial distribution south the jet and constant**
558   **meridional gradient north the jet.**